Giant Atomic Swirl in Graphene Bilayers with Biaxial Heterostrain

Florie Mesple, Niels R. Walet, Guy Trambly de Laissardière, Francisco Guinea, Djordje Došenović, Hanako Okuno, Colin Paillet, Adrien Michon, Claude Chapelier, and Vincent T. Renard*

The study of moiré engineering started with the advent of van der Waals heterostructures, in which stacking 2D layers with different lattice constants leads to a moiré pattern controlling their electronic properties. The field entered a new era when it was found that adjusting the twist between two graphene layers led to strongly-correlated-electron physics and topological effects associated with atomic relaxation. A twist is now routinely used to adjust the properties of 2D materials. This study investigates a new type of moiré superlattice in bilayer graphene when one layer is biaxially strained with respect to the other—so-called biaxial heterostrain. Scanning tunneling microscopy measurements uncover spiraling electronic states associated with a novel symmetry-breaking atomic reconstruction at small biaxial heterostrain. Atomistic calculations using experimental parameters as inputs reveal that a giant atomic swirl forms around regions of aligned stacking to reduce the mechanical energy of the bilayer. Tight-binding calculations performed on the relaxed structure show that the observed electronic states decorate spiraling domain wall solitons as required by topology. This study establishes biaxial heterostrain as an important parameter to be harnessed for the next step of moiré engineering in van der Waals multilayers.

1. Introduction

The physics of moiré materials is driven by the details of the relative arrangement of 2D layers stacked on top of each other. The emblematic example is twisted bilayer graphene (TBG), which evolves from two independent layers for rotation angles larger than 10°[1,2] to a flat-band material showing strongly correlated electron physics near the magic angle of 1.1°.[3,4] For angles smaller than the magic one, domain wall solitons with topological 1D electronic states[5–7] form to minimize the stacking energy.[8–10] This rich physics is determined by a single parameter: the twist angle between the layers that can be controlled precisely in the tear and stack technique.[11] Yet, it is also possible to change the relative arrangement of graphene layers using heterostrain, the deformation of one layer with respect to the other.[12] Until now research has largely focused on the study of non-intentional uniaxial heterostrain that broadens the flat bands[13,14] and is essential in the selection of the many-body ground states of TBG.[15] Much less attention has been devoted to biaxial heterostrain that is generally of smaller amplitude and was assumed to have a smaller effect on the physics of TBG.[16] However, bilayer graphene with pure biaxial heterostrain presents a moiré pattern with Bernal stacked (AB) and aligned (AA) regions, similar to TBG (**Figure 1**a). This moiré has sixfold symmetry but, contrary

F. Mesple, C. Chapelier, V. T. Renard
Univ. Grenoble Alpes
CEA, Grenoble INP, IRIG, PHELIQS, Grenoble 38000, France
E-mail: vincent.renard@cea.fr
N. R. Walet
Department of Physics and Astronomy
University of Manchester
Manchester M13 9PY, UK

The ORCID identification number(s) for the author(s) of this article can be found under https://doi.org/10.1002/adma.202306312

G. Trambly de Laissardière
Laboratoire de Physique Théorique et Modélisation (UMR 8089)
CY Cergy Paris Université, CNRS, Cergy-Pontoise 95302, France
F. Guinea
Imdea Nanoscience
Faraday 9, Madrid 28015, Spain
F. Guinea
Donostia International Physics Center
Paseo Manuel de Lardizábal 4, San Sebastián 20018, Spain
D. Došenović, H. Okuno
University Grenoble Alpes
CEA, IRIG-MEM, Grenoble 38054, France
C. Paillet, A. Michon
Université Côte d'Azur
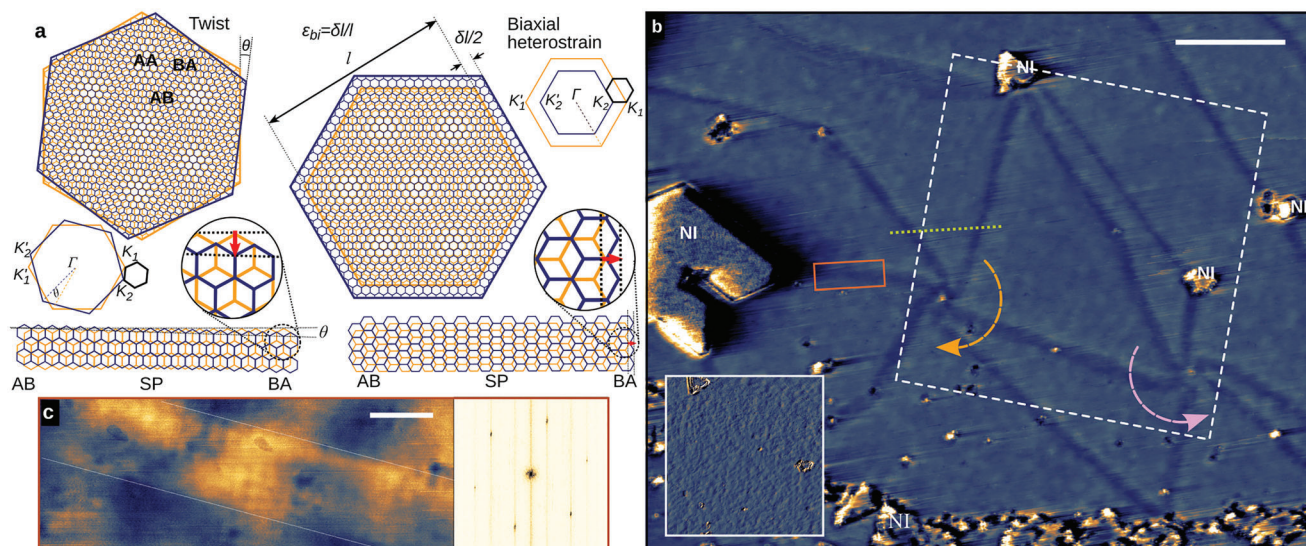CNRS, CRHEA, Rue Bernard Grégory, Valbonne 06560, France

ADVANCED
SCIENCE NEWS
www.advancedsciencenews.com

**ADVANCED
MATERIALS**
www.advmat.de

Figure 1. Soliton network in bilayer graphene on SiC. a) Schematic model of the real and reciprocal space structure of a twist moiré (left) and biaxial moiré (right) with their corresponding domain walls—of shear and tensile types, respectively. The Burgers vector (in red) characterises the DW type as it is either parallel to the DW for a shear DW or perpendicular to it for a tensile one. b) STM current image ($V_b = -300$ mV, $I_t = 250$ pA) for an intercalated surface of bilayer graphene on SiC, with a reconstructed moiré featuring an (anti-)clockwise swirling feature in (blue) orange. Non-intercalated regions are indicated by NI. Scale bar: 100 nm long. The inset shows the STM image of the area highlighted by the dotted square measured at $V_b = 900$ mV and $I_t = 250$ pA. The dotted yellow line shows the position of the line spectroscopy presented in Figure 3f. c) Enlarged view of a soliton (red rectangle in b and for the same tunneling conditions). The Fourier transform shows that the crystallographic directions (rotated by $\pi/2$ with respect to Fourier harmonics) are along the soliton direction. Scale bar: 10 nm.

to that of TBG, it is aligned with graphene's crystallographic directions.[17] Figure 1a also reveals that the domain walls (DWs) connecting Bernal stacked AB and BA regions are tensile while those of TBGs are shear. This is quantified by the orientation of the Burgers vector describing the shift of the unit cell across the DW (Figure 1a).[18] These structural differences raise the question of the electronic properties of such biaxial heterostrain moiré and whether or not they can be observed experimentally.

2. Results and Discussion

2.1. Morphology of Biaxially Heterostrained Graphene Bilayers

Figure 1b shows a scanning tunnelling microscopy (STM) image of bilayer graphene produced by hydrogen intercalation of graphene on the silicon face of 6H-SiC[19–22] (see Experimental Section for details). The surface is mostly released although a few non-intercalated (NI) regions remain (Figure 1b; Figure S1, Supporting Information). The intercalated surface features a complex network of lines similar to the soliton network observed in marginally twisted bilayer graphene (MTBG). However, here the solitons spiral around their crossing points that has not been reported in MTBG.[9,23–25] In addition, atomically resolved images (Figure 1c) show that the solitons are mostly aligned with graphene's crystallographic directions, suggesting that the layers are subject to biaxial heterostrain. The soliton length of about $a_M = 250$ nm gives an estimate of $\varepsilon_{bi} = (a_b - a_t)/a_t = a_{Gr}/a_M \approx 0.1\%$ where $a_t = a_{Gr}$ is the lattice constant of the top layer assumed to be unstrained and a_b is the lattice constant of the bottom layer. This value is consistent with previous measurements[26–28]

which concluded that strain is imposed to the bottom layer by the $6\sqrt{3} \times 6\sqrt{3}R30°$ SiC reconstruction.

2.2. Modeling of the Structural Relaxation

Previous investigations of monolayers of metallic atoms on a rigid substrate show that a small lattice mismatch can lead to such spiralling solitons.[29–32] Before we demonstrate that this is also the case for bilayer graphene, a more detailed investigation of the relative arrangement of the layers is needed. The solitons in Figure 1b do not all have the same length suggesting a uniaxial heterostrain component that varies in space. It is therefore difficult to describe the entire structure directly. Instead we model each of the triangles as a distinct commensurate structure (see Figure S2, Supporting Information). We focus on the one highlighted by the dotted square in Figure 1b, which is characterized by a biaxial heterostrain of $\epsilon_{bi} = -0.08\%$, a uniaxial heterostrain of $\epsilon_{uni} = -0.057\%$ and a twist angle of $\theta = 0.01°$. We then build a 3.5-million-atoms commensurate cell with this particular relative stacking describing a situation with homogeneous strain.[14] However, this is still not realistic because the layers relax to balance in-layer strain and interlayer atomic alignment in such a huge moiré lattice. We therefore perform an atomistic simulation minimizing the stacking and elastic energies, as detailed in the Experimental Section and ref. [10].

The resulting local stacking represented in colors in **Figure 2**a reproduces very well spiralling solitons. In principle, the relaxation can feature either spiraling or straight solitons for the same parameters (see Figure 2e for a 0.1% purely biaxial moiré). But the spiral relaxation mode dominates up to about 1.5% of strain
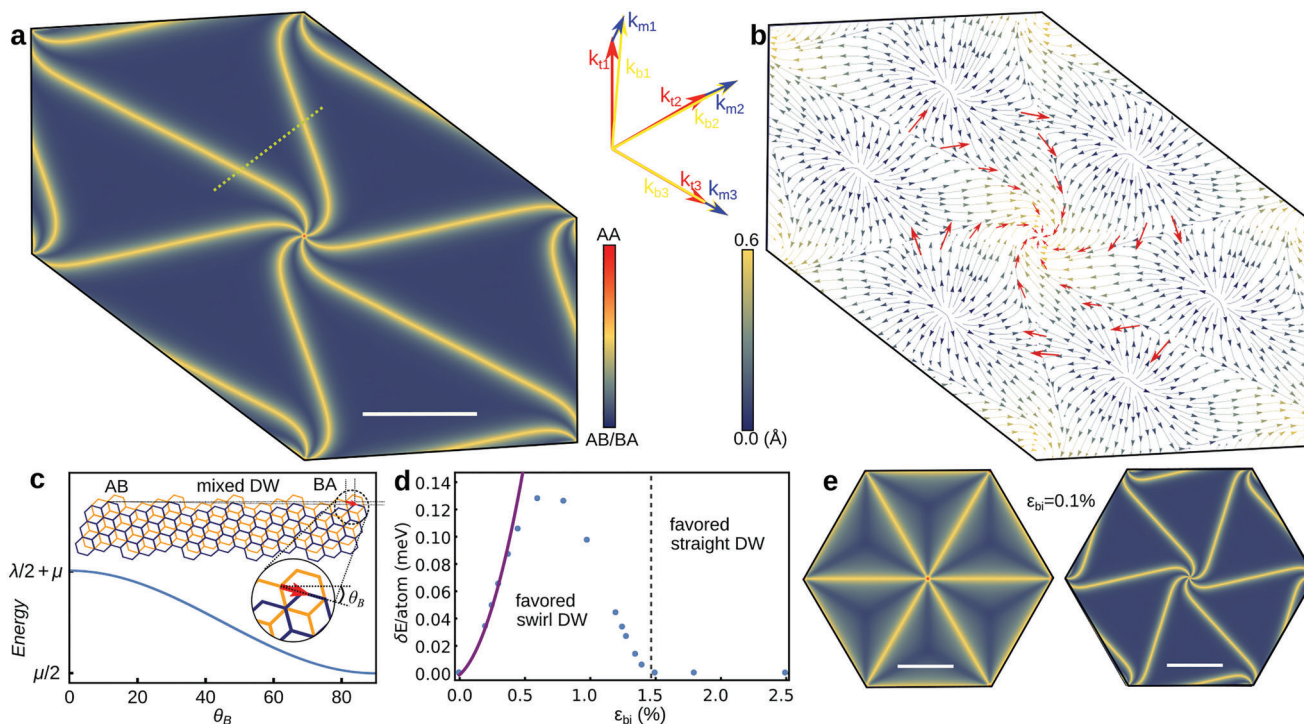
Figure 2. Structural relaxation. a) Calculated stacking parameter: blue shows AB/BA alignment, red AA, and yellow shows competing alignment. (See ref. [34] for the definition of the stacking parameter.) The dotted line shows the position of the LDOS calculations of Figure 3g. Scale bar: 100 nm. b) Atomic-flow map leading to the relaxed structure. The arrows show qualitative streamlines of one layer where lighter colors indicate larger atomic movements. In the other layer, the atoms move in the opposite direction. The red arrows indicate the local Burgers vectors along the domain walls. c) Relative stacking energy of the soliton upon variation of the soliton type, characterized by the angle between the Burgers vector and the direction perpendicular to the DW, as defined on the sketch of a DW of mixed type. d) Energetics of configurations with varying biaxial heterostrain: we show the difference between the swirl and straight solitons relaxation modes. Above $\epsilon_{bi} = 1.4\%$ (vertical dotted line), no swirl solution can be found (see Figure S3, Supporting Information). The purple line shows a simple fit for small heterostrain, and is valid only up to ≈ 0.5% strain (Figure S5b, Supporting Information). e) Stacking parameter for a relaxed structure from a moiré induced by a 0.1% purely biaxial heterostrain. Right: Low-energy swirl soliton mode; Left: Metastable straight soliton mode. Scale bars: 100 nm.

(Figure 2d). Similarly to marginally twisted graphene layers, AB regions that have lower stacking energy grow at the expense of the higher-energy AA regions, concentrating elastic strain in the solitons.[33] Interestingly, while AB regions are marginally affected by it, the spiral mode drastically reduces the surface of AA regions below $\epsilon_{bi} = 1.5\%$ (Figure S3, Supporting Information). In addition, atoms flow outward from the center of the AB regions in the top layer forming a giant atomic swirl around AA regions (Figure 2b) further reducing the elastic energy. Indeed, the swirl causes the Burger vector of the soliton (defined in Figure 2c) to rotate from perpendicular in between AA regions to parallel in AA region, which reduces its energy according to the following equation:

$$E_{\text{elas}} \propto \left[\left(\frac{\lambda}{2} + \mu \right) \cos^2\left(\theta_{\text{B}}\right) + \mu \frac{\sin^2\left(\theta_{\text{B}}\right)}{2} \right] \tag{1}$$

where λ and μ are the first and second Lamé parameters of graphene and θ_{B} the angle of the Burger vector (Figure 2c and Experimental Section for more details). Even though derived by elastic theory, this reflects the behavior at the atomic scale: in general it is harder to change bond lengths than bond angles.

Figure S4 (Supporting Information) shows that the solitons fully relax into shear type in AA region.

In addition, calculations of Figures 2a and 2e show that the spiral is mostly determined by the biaxial heterostrain component, while uniaxial heterostrain has a small effect. Relaxation restores locally the rotational symmetry near AA regions, which is lost at the scale of the unit cell due to the uniaxial heterostrain. This explains the regularity of the spiral seen in experiment despite the in-homogeneity of heterostrain and justifies our approximation of the experimental structure by the chosen unit cell. The experimental diameter of the swirl (about 100 nm) and the width of the soliton, between 15 and 35 nm depending on energy (see below), are very well reproduced (20 ± 10 nm in the theory). Figure S3 (Supporting Information) present complementary calculations of the development of the swirl as function of biaxial heterostrain. Figure 1b suggests that there exist no preferred direction for the swirl. In numerical simulations, we find both orientations depending on some random inputs that give rise to the symmetry breaking. This is clearly evidenced in Figure S5d (Supporting Information), where we show the reaction path from a left- to a right-rotating swirl, with the straight DW case as the transition state between the two, i.e., at a saddle point in the energy landscape. It is thus a classic example of spontaneous
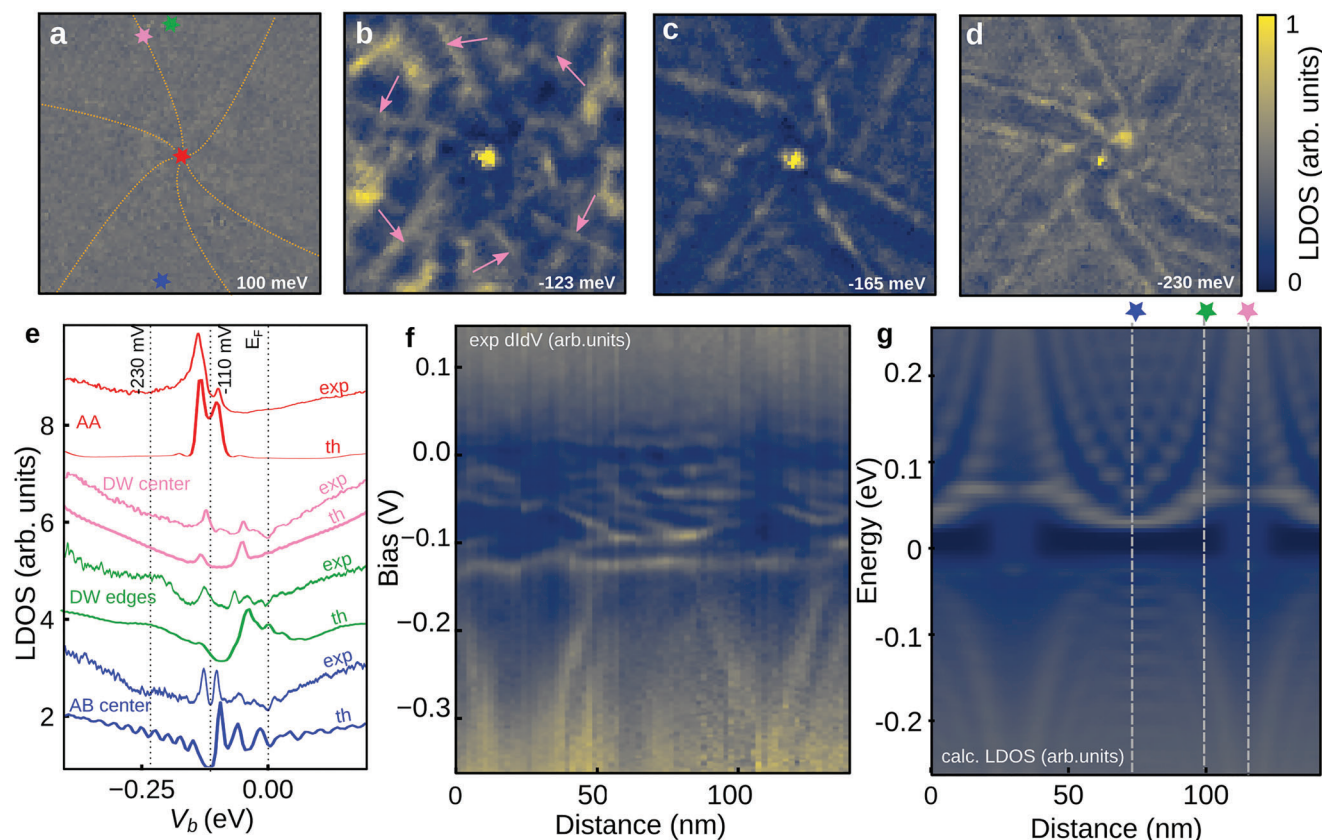
ADVANCED
SCIENCE NEWS
www.advancedsciencenews.com

ADVANCED
MATERIALS
www.advmat.de

Figure 3. Electronic properties of a marginally biaxially heterostrained graphene bilayer. a–d) Spatially resolved LDOS maps centered around the AA region, featuring energy-dependent spectroscopic features. The setpoint is (V_b = +200 mV, I_t = 250 pA). e) Corresponding individual spectra showing localized states in the AA region in red, a localized state at the center of the DW at charge neutrality in pink, and energy dependent confined states at the DW edges (green, orange). The Dirac energy E_D is shifted with respect to E_F due to the substrate induced doping. The electric field induced gap in AB regions allows to define charge neutrality at −110 meV. Each experimental spectrum is shown along its tight-binding-calculated counterpart, which describe the data well. f) Experimental LDOS along the yellow dotted line from Figure 1b that crosses two solitons. g) Corresponding tight-binding calculations, taken along the yellow dotted line defined in Figure 2a.

symmetry breaking through a pitchfork bifurcation, caused by the applied heterostrain.[35,36] As a final verification we checked that no swirl is obtained in the calculations of a twist moiré (see Figure S7, Supporting Information). All in all, the theoretical results together with the interpretation of the experimental images firmly establish that we have indeed observed a marginally biaxially heterostrained graphene bilayer.

2.3. Solitonic Electronic States

Interestingly, while the soliton network is visible at negative energies, the STM image is essentially featureless at positive energy (Figure 1b; Figure S8, Supporting Information). This strongly suggests that solitonic features seen in STM are of electronic origin calling for a detailed study. **Figure 3**a–d show local-density-of-states (LDOS) maps determined from a differential conductance spectrum measured at each pixel (see Experimental Section and supplementary animations for the full energy dependence of the maps). The measurements are centred on the central spiral in Figure 1b. The sequence of energy-resolved images reveal a complex spatial dependence of the spectroscopic features. First of all,

AB regions far from the solitons show two resonances that we attribute to an electronic gap opened in AB region by the electric field induced by the substrate (Figure 3e, blue). This allows us to determine a gap of E_g = 27 meV and charge neutrality point at E_D = −110 meV, both of which are typical of bilayer graphene on SiC.[37–40] We also note a V-shaped depression of the experimental density of states at the Fermi energy E_F, which we attribute to the tunnelling anomaly in 2D systems[41] (see also Figure 3f). A strong pair of peaks indicative of resonance is found at E_D in the center of the swirl. The corresponding spectrum shown in Figure 3b (red) strongly resembles the localization peak seen in AA regions of TBG.[2,42] Below charge neutrality, we observe a set of edge-state-like (ESL) features flanking the solitons and moving toward it as energy is decreased Figure 3c,d. These lead to an energy-dependent effective width of the soliton seen in STM images and correspond to broad resonances in individual spectra (Figure 3e, green). Similar features were already reported in TBG and attributed to either van Hove singularities,[43] or to pseudo Landau Levels induced by the inhomogeneous strain concentrated at the DW.[44] We exclude these interpretations here because of the broad spatial extension and highly dispersive nature of the ESL.

ADVANCED
SCIENCE NEWS
www.advancedsciencenews.com

ADVANCED
MATERIALS
www.advmat.de

In order to get more insight into these spectral features, we perform tight-binding calculations using the relaxed unit cell shown in Figure 2a, including a 30 meV potential difference between the layers as in the experiment (see Experimental Section and ref. [42] for details on TB calculations). The local density of states calculated in the top layer reproduces well the experimental one (Figure 3e). However they do not shed light on the origin of ESL features, and we show the full spatial dependence along a line crossing the unit cell in Figure 3f (experiments) and Figure 3g (theory). Away from E_F, the local density of states reveals confined states in the AB regions, which express more intensely above charge neutrality, and are reminiscent of a 2D electron gas confined by hard walls.[45] The confinement originates from the reflection of electrons by the tensile domain wall, which occurs up to high energies at normal incidence for tensile solitons.[46,47] It is interesting that the present soliton has a rotating Burgers vector, which does not seem to affect the confinement and will deserve further theoretical attention. Another interesting feature is that below E_D, only the first interference oscillations decorate the confinement regions and disperse like ESL features in experiments. This particle-hole asymmetry is reproduced in the calculations. At $E > E_D$ the localized states manifest as sharp resonances distributed on the entire AB region with a characteristic length scale (Figure S9, Supporting Information and supplementary animation for the full energy dependence of the maps), which are not perfectly periodic because of the irregularity of the confining region and fluctuations of the Fermi level. Noteworthy, the LDOS is featureless above E_F as expected from STM images.

Finally, we address the question of the states located in the soliton's core. These are emphasized in Figure 3b,e (pink arrows and LDOS spectrums) and well captured in our tight-binding calculations that include both heterostrain and relaxation. They are slightly obscured in the experiment due to the strong confinement features in the neighboring AB regions at the same energies. Topology requires the presence of helical states in such channels created by the solitons at the AB/BA boundary.[5–7] It is therefore tempting to attribute these core states to helical states. However, helical states, which are not topologically protected could possibly hybridize with the bulk states.[10] Moreover, it is not clear what is the impact of the pseudomagnetic field that arises due to the strain gradient and which will certainly have a peculiar texture in the spiraling soliton. This will deserve more theoretical investigations with a phenomenological model including both hybridization and pseudomagnetic field.

3. Conclusions

Biaxial heterostrain offers a new moiré platform to study localization and topological solitons. Its interplay with other parameters such as twist angle and large uniaxial heterostrain should be investigated more systematically. Also, even if our study demonstrates that in-plane atomic movement is the main driver of our observation, out of plane relaxation will have to be considered. This will require a much more involved, and not so well established, tight-binding model[34] (see also ref. [48, 49] for related works in TBG). From the experimental perspective, we have exploited the native biaxial heterostrain in intercalated bilayer graphene on SiC that is certainly stabilized by non intercalated regions. Experiments in trilayer graphene[50] and WS$_2$[51] with

similar morphology indicate that the atomic swirl also occurs in other van de Waals stacks under appropriate conditions and this is supported by very recent calculations[52] in MoX$_2$/WX$_2$ (TMDs with X = S or Se). A more systematic study will require to control biaxial heterostrain as was recently demonstrated in ref. [53]. We anticipate that the combined choice of material, twist angle, heterostrain and pressure will bring moiré engineering to its full potential.

4. Experimental Section

Sample Fabrication: The sample was grown by propane-hydrogen chemical vapor deposition (CVD) on the Si-face of 6H-SiC.[19] During the whole process, SiC was exposed to a 91%Ar 9%H$_2$ mixture at a pressure of 800 mbar. After a 5 min temperature ramp, propane was added to the gas phase for a 15 min growth plateau at 1550 °C, and finally, the sample was cooled to room temperature without propane within 20 min. This process could be compared to the Si-sublimation method. However, under hydrogen, carbon from SiC cannot be segregated on the surface, making an external carbon source mandatory to grow graphene.[20] Nevertheless, for the growth conditions specified above, the graphene film was very similar to what could be obtained using Si-sublimation, i.e., a monolayer graphene resting on a buffer layer on SiC.[21] This buffer layer was made of carbon atoms arranged in an honeycomb lattice similar to graphene, but containing a significant fraction of sp^3 carbon atoms covalently bonded to SiC. These bonds could be detached by intercalating Hydrogen atoms below the buffer layer, which produced a quasi-free-standing bilayer graphene.[22] In this work the intercalation was done by a 30 min annealing under a H$_2$/NH$_3$ gas mixture at 150 mbar and at a temperature of 1100 °C.

Scanning Tunnelling Microscopy and Spectroscopy: The measurements were acquired using a homebuilt STM in a cryogenic environment at 4.2 K that ensures a ≈ 1.5 meV resolution on spectroscopic measurements. Each measurement is identified with its setpoint: the bias voltage V_b and tunnelling current I_t at the start of the bias sweep. The spectroscopic measurements were recorded using phase sensitive detection with a 4mV AC voltage modulation. The density of state maps were obtained from grid spectroscopy—or current-imaging tunnelling spectroscopy (CITS). At each pixel, the feedback loop was switched off at the setpoint conditions and a sweep over the bias voltage was performed while recording the dI/dV signal. All microscopic images and CITS data were analyzed using Gwyddion[54] and Scanning Tunneling Microscopy analysis in Python (STMaPy), a data analysis tool written in Python by some of the authors.[55]

Local Commensurably Analysis of the Moiré Swirl Pattern: The STM images revealed a moiré with a very large periodicity, thus associated with atomic relaxation and atomic reconstruction phenomena. Nevertheless, the dimensions of the moiré could be associated with the corresponding unrelaxed stacking. Following refs. [12, 56], the relative stacking is described by the twist $\theta_{int} = \theta$ between the layers, uniaxial ϵ_{uni} and biaxial ϵ_{bi} heterostrain. The analysis of the moiré length had to be combined with an analysis of the local crystallographic directions of graphene in order to find a unique stacking. These could be determined exactly from atomically resolved STM images, which was spatially homogeneous, with variations of 0.5° at the DWs, where strain was concentrated by the reconstruction.

In practice, one has to solve the following equation :

$$\begin{pmatrix} \vec{k}_{b_1} \\ \vec{k}_{b_2} \end{pmatrix} = \begin{pmatrix} a & c \\ b & d \end{pmatrix} \begin{pmatrix} \vec{k}_{t_1} \\ \vec{k}_{t_2} \end{pmatrix} \tag{2}$$

where the top layer periodicity in reciprocal space $\vec{k}_{t_i}$, $i = 1$, 2 is determined from atomically resolved STM images, and the bottom layer periodicity $\vec{k}_{b_i}$ is determined from the first order commensurably equation $\vec{k}_{b_i} = \vec{k}_{t_i} + \vec{k}_{m_i}$ where $\vec{k}_{m_i}$ is the moiré period of a given triangle determined from large scale images.

This relative stacking was described by the so called Park–Madden matrix as introduced in ref. [56] and used in refs. [12, 14], which describes the relative stacking of the layers. Experimental *a*, *b*, *c*, and *d* could be related to the rotation between the layers and heterostrain. The moiré size was set by the values of pure twist and biaxial heterostrain between the layers while the anisotropy of the moiré was characterized by the uniaxial heterostrain. Note that such big moiré lengths were very sensitive to the relative stacking variables, and so those variables were found by imposing the exact moiré size required.

Because of the high inhomogeneity of the moiré, the analysis is performed for each closed triangle of the moiré as shown in Figure S2 (Supporting Information), where the relative stacking including twist and heterostrain were attributed to each individual triangle.

Note that this analysis describes the unrelaxed stacking of the moiré, which was locally modified upon relaxation, concentrating strain at the DWs and around the AA-stacking region and maximizing the surface area of AB and BA stacked regions.

Calculations of Relaxation: From the Park–Madden matrix as derived from previous section, the method presented in ref. [14] was used to produce a commensurate cell describing the unrelaxed relative stacking between the layers. The lowest energy relaxed configuration is found using molecular dynamic calculations using LAMMPS.[57] These calculations minimize binding and elastic energy of the layers by allowing in-plane movements of atoms. The method and ideas specific to graphene were discussed in ref. [34], as well as references cited therein. It used the reactive empirical bond order (REBO) potential to describe intralayer interactions,[58] and the Kolmogorov–Crespi[59] potential to describe the interlayer interactions. Even though the global effect of the relaxation were large, the most an individual atom was displaced in plane was 0.6 Å. More details on these displacements are shown in Figure S6 (Supporting Information).

Tight-Binding: All tight-binding calculations in this paper use parameters that had been determined previously[60] and show good agreement with experimental data.[12,14] With these parameters, the Fermi velocity in a monolayer is $v_{mono} = 1.1 \times 10^6$ m s^{-1}. In AB/BA bilayers, the sublattice asymmetry was significant in the LDOS spectra for energies below 450 meV as the lowest energy dispersive bands were localized on the non-dimer atoms of the layers (A_1/B_2 or A_2/B_1); see Figure S9 (Supporting Information) for more insight. The LDOS calculations shown in this work correspond the averaged LDOS between the A and B sublattices, using a 5 meV Gaussian broadening. In addition, a 30 meV potential difference between the layers was included, to correspond to the experimental situation.

Energy of the Soliton: The relaxation calculations show that the giant atomic swirl originated from a rotation of the Burgers vectors of the DW as the soliton varied from a tensile type to a shear type. Normally, a shear type soliton was energetically favored, as it required a smaller modification of the carbon–carbon bond lengths.

This could be modeled by a continuous local displacement **u** of the atoms along a soliton, expressed in terms of the displacement along the soliton as given by the function $f(x)$, modulated by the direction of their displacement as defined by θ_B, the angle of the Burgers vector with respect to the DW direction. This angle characterised the soliton type, which ranged from purely tensile ($\theta_B = 0$) to purely shear ($\theta_B = \pi/2$)

$$(u_x(x), u_y(x)) = (f(x) \cos(\theta_B), f(x) \sin(\theta_B)) \quad (3)$$

where the total displacement across the soliton dislocation satisfies

$$f(x) = \begin{cases} -\frac{d}{2\sqrt{3}} & x \to -\infty \\ \frac{d}{2\sqrt{3}} & x \to \infty \end{cases} \quad (4)$$

The corresponding local strain along the soliton can be written as

$$(\partial_x u_x(x), \partial_x u_y(x)) = (f'(x) \cos(\theta_B), f'(x) \sin(\theta_B)) \quad (5)$$

Using the fact that the elastic energy of a two dimensional solid is given by

$$E_{elas} = \frac{\lambda}{2} \int_{-\infty}^{\infty} (\partial_x u_x(x))^2 dx + \mu \int_{-\infty}^{\infty} \left[(\partial_x u_x(x))^2 + (\partial_x u_y(x))^2 \right]^2 dx \quad (6)$$

It finds that the soliton's energy per unit length is given by

$$E_{elas} = \left[\lambda \frac{\cos^2(\theta_B)}{2} + \mu \cos^2(\theta_B) + \mu \frac{\sin^2(\theta_B)}{2} \right] \times \int_{-\infty}^{\infty} [f'(x)]^2 dx \quad (7)$$

This is the result shown in Figure 2c.

Supporting Information

Supporting Information is available from the Wiley Online Library or from the author.

Acknowledgements

Author Contributions

V.T.R., C.C., and F.M. conceived the experiments. C.P. and A.M. fabricated the samples. F.M., V.T.R., and C.C. performed and analyzed STM experiments. D.D. and H.O. performed TEM measurements. N.R.W. and F.G. produced the theoretical models of atomic relaxation and G.T.d.L. the calculations of the electronic structure. F.M. and V.T.R. wrote the manuscript with the input of all authors. V.T.R. supervised the collaboration.

Conflict of Interest

The authors declare no conflict of interest.

Data Availability Statement

The data that support the findings of this study are available from the corresponding author upon reasonable request.

Keywords

[1] J. M. B. Lopes dos Santos, N. M. R. Peres, A. H. Castro Neto, *Phys. Rev. Lett.* **2007**, *99*, 256802.

[2] G. Li, A. Luican, J. M. B. L. dos Santos, A. H. Castro Neto, A. Reina, J. Kong, E. Y. Andrei, *Nat. Phys.* **2009**, *6*, 113.

[3] Y. Cao, V. Fatemi, K. Watanabe, T. Taniguchi, E. Kaxiras, P. Jarillo-Herrero, *Nature* **2019**, *55*, 43.

[4] Y. Cao, V. Fatemi, S. Afng, K. Watanabe, T. Taniguchi, E. Kaxiras, P. Jarillo-Herrero, *Nature* **2019**, *556*, 80.

[5] P. San-Jose, E. Prada, *Phys. Rev. B* **2013**, *88*, 121408.

[6] F. Zhang, A. H. MacDonald, E. J. Mele, *Proc. Nat. Acad. Sci. USA* **2013**, *110*, 10546.

[7] P. Rickhaus, J. Wallbank, S. Slizovskiy, R. Pisoni, H. Overweg, Y. Lee, M. Eich, M.-H. Liu, K. Watanabe, T. Taniguchi, T. Ihn, K. Ensslin, *Nano Lett.* **2018**, *18*, 6725.

[8] M. M. van Wijk, A. Schuring, M. I. Katsnelson, A. Fasolino, *2D Mater.* **2015**, *2*, 034010.

[9] J. S. Alden, A. W. Tsen, P. Y. Huang, R. Hovden, L. Brown, J. Park, D. A. Muller, P. L. McEuen, *Proc. Nat. Acad. Sci. USA* **2013**, *110*, 11256.

[10] N. R. Walet, F. Guinea, *2D Mater.* **2019**, *7*, 015023.

[11] K. Kim, M. Yankowitz, B. Fallahazad, S. Kang, H. C. P. Movva, S. Huang, S. Larentis, C. M. Corbet, T. Taniguchi, K. Watanabe, S. K. Banerjee, B. J. LeRoy, E. Tutuc, *Nano Lett.* **2016**, *16*, 1989.

[12] L. Huder, A. Artaud, T. L. Quang, G. T. de Laissardière, C. Chapelier, V. T. Renard, *Phys. Rev. Lett.* **2018**, *120*, 156405.

[13] Z. Bi, N. F. Q. Yuan, L. Fu, *Phys. Rev. B* **2019**, *100*, 035448.

[14] F. Mesple, A. Missaoui, T. Cea, L. Huder, F. Guinea, G. Trambly de Laissardière, C. Chapelier, V. T. Renard, *Phys. Rev. Lett.* **2021**, *127*, 126405.

[15] K. P. Nuckolls, R. L. Lee, M. Oh, D. Wong, T. Soejima, J. P. Hong, D. Călugăru, J. Herzog-Arbeitman, B. A. Bernevig, K. Watanabe, T. Taniguchi, N. Regnault, M. P. Zaletel, A. Yazdani, arXiv: 2303.00024, v1, **2023**.

[16] N. Nakatsuji, M. Koshino, *Phys. Rev. B* **2022**, *105*, 245408.

[17] M. V. der Donck, C. D. Beule, B. Partoens, F. M. Peeters, B. V. Duppen, *2D Mater.* **2016**, *3*, 035015.

[18] A. Vaezi, Y. Liang, D. H. Ngai, L. Yang, E.-A. Kim, *Phys. Rev. X* **2013**, *3*, 021018.

[19] A. Michon, S. Vézian, A. Ouerghi, M. Zielinski, T. Chassagne, M. Portail, *Appl. Phys. Lett.* **2010**, *97*, 171909.

[20] R. Dagher, E. Blanquet, C. Chatillon, T. Journot, M. Portail, L. Nguyen, Y. Cordiera, A. Michon, *CrystEngComm* **2018**, *20*, 3702.

[21] B. Jabakhanji, A. Michon, C. Consejo, W. Desrat, M. Portail, A. Tiberj, M. Paillet, A. Zahab, F. Cheynis, F. Lafont, F. Schopfer, W. Poirier, F. Bertran, P. Le Fèvre, A. Taleb-Ibrahimi, D. Kazazis, W. Escoffier, B. C. Camargo, Y. Kopelevich, J. Camassel, B. Jouault, *Phys. Rev. B* **2014**, *89*, 085422.

[22] C. Riedl, C. Coletti, T. Iwasaki, A. A. Zakharov, U. Starke, *Phys. Rev. Lett.* **2009**, *103*, 246804.

[23] H. You, R. Engelke, S. Carr, S. Fang, K. Zhang, P. Cazeaux, S. H. Sung, R. Hovden, A. W. Tsen, T. Taniguchi, K. Watanabe, G.-C. Yi, M. Kim, M. Luskin, E. B. Tadmor, E. Kaxiras, P. Kim, *Nat. Mater.* **2019**, *18*, 448.

[24] D. Halbertal, N. R. Finney, S. S. Sunku, A. Kerelsky, C. Rubio-Verdú, S. Shabani, L. Xian, S. Carr, S. Chen, C. Zhang, L. Wang, D. Gonzalez-Acevedo, A. S. McLeod, D. Rhodes, K. Watanabe, T. Taniguchi, E. Kaxiras, C. R. Dean, J. C. Hone, A. N. Pasupathy, D. M. Kennes, A. Rubio, D. N. Basov, *Nat. Commun.* **2021**, *12*, 242.

[25] T. A. de Jong, T. Benschop, X. Chen, E. E. Krasovskii, M. J. A. de Dood, R. M. Tromp, M. P. Allan, S. J. van der Molen, *Nat. Commun.* **2022**, *13*, 70.

[26] A. Michon, L. Largeau, O. Mauguin, A. Ouerghi, S. Vézian, D. Lefebvre, E. Roudon, M. Zielinski, T. Chassagne, M. Portail, *Phys. Status Solidi C* **2012**, *9*, 175.

[27] F. Giannazzo, I. Shtepliuk, I. G. Ivanov, T. Iakimov, A. Kakanakova-Georgieva, E. Schiliró, P. Fiorenza, R. Yakimova, *Nanotechnology* **2019**, *30*, 284003.

[28] T. A. de Jong, L. Visser, J. Jobst, R. M. Tromp, S. J. van der Molen, *Phys. Rev. Mater.* **2023**, *7*, 034001.

[29] J. Barth, R. Behm, G. Ertl, *Surf. Sci.* **1994**, *302*, L319.

[30] C. Günther, J. Vrijmoeth, R. Q. Hwang, R. J. Behm, *Phys. Rev. Lett.* **1995**, *74*, 754.

[31] M. Corso, L. Fernández, F. Schiller, J. E. Ortega, *ACS Nano* **2010**, *4*, 1603.

[32] S. Quan, L. He, Y. Ni, *Phys. Chem. Chem. Phys.* **2018**, *20*, 25428.

[33] M. M. van Wijk, A. Schuring, M. I. Katsnelson, A. Fasolino, *2D Mater.* **2015**, *2*, 034010.

[34] F. Guinea, N. R. Walet, *Phys. Rev. B* **2019**, *99*, 205134.

[35] R. Engelke, H. Yoo, S. Carr, K. Xu, P. Cazeaux, R. Allen, A. M. Valdivia, M. Luskin, E. Kaxiras, M. Kim, J. H. Han, P. Kim, arXiv:2207.05276, v2, **2022**.

[36] P. Cazeaux, D. Clark, R. Engelke, P. Kim, M. Luskin, arXiv: 2211.12274, v2, **2023**.

[37] G. M. Rutter, N. P. Guisinger, J. N. Crain, E. A. A. Jarvis, M. D. Stiles, T. Li, P. N. First, J. A. Stroscio, *Phys. Rev. B* **2007**, *76*, 235416.

[38] P. Lauffer, K. V. Emtsev, R. Graupner, T. Seyller, L. Ley, S. A. Reshanov, H. B. Weber, *Phys. Rev. B* **2008**, *77*, 155426.

[39] A. Bostwick, J. McChesney, T. Ohta, E. Rotenberg, S. T., K. Horn, *Prog. Surf. Sci.* **2009**, *84*, 380.

[40] E. Moreau, S. Godey, X. Wallart, I. Razado-Colambo, J. Avila, M.-C. Asensio, D. Vignaud, *Phys. Rev. B* **2013**, *88*, 075406.

[41] B. L. Altshuler, A. G. Aronov, P. A. Lee, *Phys. Rev. Lett.* **1980**, *44*, 1288.

[42] G. Trambly de Laissardière, D. Mayou, L. Magaud, *Nano Lett.* **2010**, *10*, 804.

[43] S. Huang, K. Kim, D. K. Efimkin, T. Lovorn, T. Taniguchi, K. Watanabe, A. H. MacDonald, E. Tutuc, B. J. LeRoy, *Phys. Rev. Lett.* **2018**, *121*, 037702.

[44] Q. Zheng, C.-Y. Hao, X.-F. Zhou, Y.-X. Zhao, J.-Q. He, L. He, *Phys. Rev. Lett.* **2022**, *129*, 076803.

[45] J.-Y. Veuillen, P. Mallet, L. Magaud, S. Pons, *J. Phys.: Condens. Matter* **2003**, *15*, S2547.

[46] M. Koshino, *Phys. Rev. B* **2013**, *88*, 115409.

[47] P. San-Jose, R. V. Gorbachev, A. K. Geim, K. S. Novoselov, F. Guinea, *Nano Lett.* **2014**, *14*, 2052.

[48] S. Dai, Y. Xiang, D. J. Srolovitz, *Nano Lett.* **2016**, *16*, 5923.

[49] T. Rakib, P. Pochet, E. Ertekin, H. T. Johnson, *Commun. Phys.* **2022**, *5*, 242.

[50] B. Lalmi, J. C. Girard, E. Pallecchi, M. Silly, C. David, S. Latil, F. Sirotti, A. Ouerghi, *Sci. Rep.* **2015**, *4*, 4066.

[51] K. Li, F. Xiao, W. Guan, Y. Xiao, C. Xu, J. Zhang, C. Lin, D. Li, Q. Tong, S.-Y. Li, A. Pan, *Nano Lett.* **2022**, *22*, 5997.

[52] M. A. Kaliteevsky, V. V. Enaldiev, V. I. Fal'ko, arXiv:2305.128848, **2023**.

[53] V. Pasquier, A. Scarfato, J. Martinez-Castro, A. Guipet, C. Renner, *Rev. Sci. Instrum.* **2023**, *94*, 013905.

[54] D. Necas, P. Klapetek, *Cent. Eur. J. Phys.* **2012**, *10*, 181.

[55] L. Huder, F. Mesple, V. T. Renard, Scanning Tunneling Microscopy Analysis in Python, **2023**, https://doi.org/10.5281/zenodo.7991365.

[56] A. Artaud, L. Magaud, T. L. Quang, V. Guisset, P. David, C. Chapelier, J. Coraux, *Sci. Rep.* **2016**, *6*, 25670.

[57] A. P. Thompson, H. M. Aktulga, R. Berger, D. S. Bolintineanu, W. M. Brown, P. S. Crozier, P. J. in 't Veld, A. Kohlmeyer, S. G. Moore, T. D. Nguyen, R. Shan, M. J. Stevens, J. Tranchida, C. Trott, S. J. Plimpton, *Comp. Phys. Comm.* **2022**, *271*, 108171.

[58] D. W. Brenner, O. A. Shenderova, J. A. Harrison, S. J. Stuart, B. Ni, S. B. Sinnott, *J. Phys.: Condens. Matter* **2002**, *14*, 783.

[59] W. Ouyang, D. Mandelli, M. Urbakh, O. Hod, *Nano Lett.* **2018**, *18*, 6009.

[60] I. Brihuega, P. Mallet, G. Trambly de Laissardière, M. M. Ugeda, L. Magaud, J. M. Gómez-Rodriguez, F. Yndurain, J.-Y. Veuillen, *Phys. Rev. Lett.* **2012**, *109*, 19680.